A riming-dependent parameterization of scattering by snowflakes using the self-similar Rayleigh–Gans approximation

Nina Maherndl, Maximilian Maahn, Frédéric Tridon, Jussi Leinonen, Davide Ori, Stefan Kneifel

Received: 6 October 2022 | Revised: 23 June 2023 | Accepted: 18 August 2023

DOI: 10.1002/qj.4573

Quarterly Journal of the Royal Meteorological Society RMetS

RESEARCH ARTICLE

A riming-dependent parameterization of scattering by snowflakes using the self-similar Rayleigh–Gans approximation

Nina Maherndl[1] | **Maximilian Maahn**[1] | **Frederic Tridon**[2,3] | **Jussi Leinonen**[4] | **Davide Ori**[5] | **Stefan Kneifel**[6]

[1]Leipzig Institute for Meteorology, Leipzig University, Leipzig, Germany

[2]Laboratoire de Météorologie Physique, University Clermont Auvergne, Clermont-Ferrand, France

[3]Department of Environment, Land and Infrastructure Engineering, Politecnico of Torino, Torino, Italy

[4]Federal Office of Meteorology and Climatology MeteoSwiss, Locarno-Monti, Switzerland

[5]Institute for Geophysics and Meteorology, University of Cologne, Cologne, Germany

[6]Meteorological Institute, Ludwig-Maximilians-University Munich, Munich, Germany

Correspondence
Nina Maherndl, Leipzig Institute for Meteorology, Leipzig University, Leipzig, Germany.
Email: nina.maherndl@uni-leipzig.de

Funding information
Deutsche Forschungsgemeinschaft, Grant/Award Numbers: 268020496-TRR 172, 408012686-SPP 2115, 492274454, SCHE 2074/1-1; U.S. Department of Energy, Grant/Award Number: DESC001796

Abstract

Riming is a key process of precipitation formation in ice-containing clouds, but quantifying riming from observations is challenging, limiting our ability to evaluate the riming process in numerical weather models. One challenge for radar observations is that riming changes both the physical properties (mass, area cross-section) and scattering properties of ice particles. These changes need to be implemented consistently as a function of riming in radar forward operators, which are required for retrievals and model evaluation in observation space. In this study, mass–size, cross-section area–size, and backscattering cross-section relations are developed as a function of the normalized rime mass for aggregates composed of various monomer types (columns, dendrites, needles, plates, and rosettes). The proposed framework allows us to simulate scattering properties of aggregated ice particles consistently as a function of riming in retrievals and radar forward operators. The parameterizations are developed from a large data set of simulated rimed aggregates of different sizes and monomer crystal types. The backscattering cross-section parameterization (the "riming-dependent parameterization") is evaluated for radar frequencies of 35.6 and 94.0 GHz and is based on the Self-Similar Rayleigh–Gans approximation (SSRGA), which is increasingly used to calculate microwave scattering of ice crystals and snowflakes. Compared with parameterizations from the literature that do not consider riming, the riming-dependent parameterization leads to significantly smaller biases in terms of backscattering cross-section. When using the particle masses and scattering properties of the individual particles simulated by the aggregation and riming model as a reference, the bias of our parameterization is below 1 dB when integrating over an exponential particle size distribution with sizes from 0.1–10 mm.

KEYWORDS

aggregates, cloud, microwave, radar, riming, scattering, self-similar Rayleigh–Gans approximation

1 | INTRODUCTION

Most precipitation on Earth is formed in ice-containing clouds, except over the subtropical oceans (Mülmenstädt *et al.*, 2015). The accurate characterization of processes involving the ice phase is therefore highly relevant for constraining the global hydrological cycle. One key process in the formation of precipitation, besides aggregation and depositional growth, is riming. Riming occurs when supercooled liquid water droplets (SLW) come into contact with ice particles, freezing onto them almost instantly. Typically, riming leads to denser, more spherical ice particles with increased mass, size, surface roughness (at least initially) and terminal fall velocity (Heymsfield, 1982; Erfani and Mitchell, 2017; Seifert *et al.*, 2019). In middle to high latitudes, riming was found to contribute significantly to snowfall rate. Moisseev *et al.* (2017) showed that, in Hyytiälä (Finland), riming was responsible for 5%–40% of snowfall mass during winter 2014/2015, whereas Harimaya and Sato (1989) found riming proportions above 50% for snowfall in a Japanese seaside area in 1987.

Quantitative observations of riming are difficult to obtain and hard to compare. One reason is that different approaches on how to quantify riming have been proposed in the literature. Mosimann *et al.* (1994) presented the degree of riming, which describes the coverage of ice particles by rime visually. They further derived the rime mass fraction (FR) from the degree of riming. FR is the fraction of total particle mass gained by riming and is commonly used in numerical weather prediction models (Morrison and Milbrandt, 2015). Leinonen and Szyrmer (2015) presented an aggregation and riming model based on various monomer types, where riming is quantified by the effective liquid water path (ELWP), the physical liquid water path (LWP) along a particle's trajectory assuming riming efficiency = 1. Mason *et al.* (2018) introduced the density factor r, which measures riming on a scale from 0, meaning unrimed (assuming the widely used mass–size relation by Brown and Francis, 1995), to 1, meaning spheres of solid ice. Using an extension of the same aggregation and riming model described by Leinonen and Szyrmer (2015), Seifert *et al.* (2019) proposed new parameterizations for the geometry of rimed aggregates and introduced the normalized rime mass M. M is defined as the ratio of rime mass and the mass of a spherical graupel particle with the same maximum dimension as the rimed particle assuming a graupel density of $700\,\mathrm{kg}\cdot\mathrm{m}^{-3}$ in the "high-density rime scenario" (Seifert *et al.*, 2019).

Radar observations have been used to quantify riming (e.g., Mosimann, 1995; Kneifel and Moisseev, 2020; Mech *et al.*, 2020; Vogl *et al.*, 2022), but most retrievals of a measure for riming are based on assumptions about particle scattering properties and how they relate to particle size, mass, and shape. These properties cannot be obtained unambiguously from radar measurements alone, because ice and snow particle geometry is highly variable in nature and exact mathematical descriptions for physical properties such as particle mass and area do not exist. Furthermore, it would not be practicable to describe each particle individually when looking at an ensemble of particles commonly observed, for example, by radar. It is therefore common practice to describe the particle geometry by relating particle size to particle mass and cross-sectional area. These relations are typically described by power laws with two parameters. Because riming strongly impacts a particle's density and therefore its mass–size relationship, it is especially important to characterize the mass–size parameter accurately in the case of riming processes.

Besides physical particle properties, particle scattering properties also need to be estimated in retrievals. The Rayleigh–Gans Approximation (RGA) provides an accurate approximation of scattering properties for unrimed ice and snow particles when compared with the computationally more expensive Discrete Dipole Approximation (DDA, Tyynelä *et al.*, 2013). RGA is based on the assumption that the electromagnetic interaction between the different parts of the scatterer is negligible with respect to the direct forcing of the external electromagnetic wave (Bohren and Huffman, 1983 pp. 158–165). In recent years, innovative scattering methods that allow moderation of the cost of computing the scattering properties of snowflake aggregates have been developed (McCusker *et al.*, 2021). Such methods, however, are still limited by the need to calculate the scattering properties of snow based on individual particle shapes and to neglect the statistical common properties of large snowflake ensembles. Based on RGA, Hogan and Westbrook (2014) presented analytic expressions to calculate scattering properties of an ensemble of ice and snow particles by assuming fractal (self-similar) structures. This formed the basics of the Self-Similar Rayleigh–Gans Approximation (SSRGA), which was further improved by Hogan *et al.* (2017) and is formulated with five dimensionless parameters α_e, κ, β, γ, ζ_1, which describe the internal mass distribution of the particles. In this study, we refer to α_e, κ, β, γ, ζ_1 as the "SSRGA parameters". SSRGA is much faster and more convenient to use than DDA and T-Matrix (Mishchenko, 2000) and offers more realistic results than Mie theory (Mie, 1908; Bohren and Huffman, 1983) or T-Matrix for computing millimetre-wave scattering and particles larger than the wavelength (Hogan *et al.*, 2017). A drawback of using SSRGA is that polarization-dependent scattering can only be predicted to a limited extent, due to the neglect of coupling between dipoles in RGA.

When applying SSRGA in radar forward operators, the SSRGA parameters proposed by Hogan and Westbrook (2014) or Hogan *et al.* (2017) are commonly used (e.g., Maahn and Löhnert, 2017; Mason *et al.*, 2019; Mech *et al.*, 2020). However, these values were calculated for unrimed ice and snow particles and can lead to high biases in the radar backscattering cross-section when applied to rimed particles, as we will show in this work. Since SSRGA parameters depend on the statistical distribution of masses within the particle, their value cannot be considered equal for particle populations with different degrees of riming. Hogan *et al.* (2017), Leinonen *et al.* (2018), and Ori *et al.* (2021) showed how SSRGA parameters depend on the properties of the ensemble of ice and snow particles used for their derivation. A consistent expression of the particle's physical and scattering properties as a function of riming is therefore a crucial step to improve radar retrievals, but also radar forward operators for atmospheric models.

Because riming typically increases density and a higher density is expected to lead to more interactions of the different parts of the scatterer, it is important to study the validity of the underlying RGA when using SSRGA in riming retrievals. In this sense, a simulator of riming at the process scale, as was presented in Leinonen and Szyrmer (2015), provides a useful tool to investigate this question. Based on such a simulator, Leinonen *et al.* (2018) found that, while the difference in backscattering cross-section of RGA versus DDA can be large for individual rimed particles, average biases stay below 1 dB for all but the most heavily rimed aggregates. In addition, they calculated the SSRGA parameters and showed that SSRGA approximates RGA well at all degrees of riming. In order to show that average scattering properties calculated by RGA provide accurate results except for heavily rimed particles, Leinonen *et al.* (2018) used ELWP as a measure for riming. The normalized rime mass M, the quantitative proxy for riming used in this study for reasons described below, does not follow a linear correlation with ELWP. Larger particles have smaller M than smaller particles at the same ELWP values. It is therefore required to reevaluate the applicability of RGA for rimed aggregates, when M is used as a measure of riming. Furthermore, previous studies did not present a parameterization of the SSRGA parameter as a function of M, or any other measure of riming, to the authors' knowledge.

This study aims at formulating a parameterization of the SSRGA parameters α_e, κ, β, γ, ζ_1 as defined by Hogan *et al.* (2017) and the mass– and area–size parameters a_m, b_m, and a_A, b_A by a physically meaningful parameter of riming. The SSRGA parameters describe the statistical properties of the internal mass distribution of the particles; the a and b parameters are the prefactors and exponents in the mass– and area–size power laws. For quantifying riming, we select M, because, in opposition to the degree of riming, r and, to an extent, ELWP, M has the advantage of being a physically well-defined quantity. Another advantage of clustering rimed aggregates with respect to M compared with other riming measures including FR is that it allows us to derive mass–size relations providing more realistic fall velocities for moderately rimed aggregates (Tridon *et al.*, 2022). M can also be calculated from the rime mass and the size distribution used to represent ice-phase particles in the new predicted particle properties (P3) scheme, a bulk microphysics scheme for atmospheric models proposed by Morrison and Milbrandt (2015). In P3, ice particles are not separated into distinct classes, but described as a single ice-phase category, with the advantage that, for example, the mass–size relation can be varied continuously.

The developed framework presented in this study allows us to estimate backscattering cross-sections for arbitrary M values consistently. Using the aggregation and riming model described in Leinonen *et al.* (2013), Leinonen and Szyrmer (2015), and Leinonen and Moisseev (2015), we simulated a large data set of rimed aggregates of different sizes and monomer shapes, which we binned by M. SSRGA parameters were calculated for different riming degrees and their relationship to M was analysed. Through fits, empirical relations of α_e, κ, β, γ, ζ_1 as functions of only M were obtained (Section 2.4). We show the applicability of RGA compared with DDA for different M (Section 3.1) as well as SSRGA compared with DDA (Section 3.2), before we compare radar backscattering cross-section bias for 35.6 GHz (Ka band) and 94.0 GHz (W band) using our proposed SSRGA parameterization compared with using literature values (Section 3.3). We analyse biases for both individual particles (Section 3.3.1) and size distributions (Section 3.3.2). In addition, we present mass and area–size relationships obtained for different monomer types (columns, dendrites, needles, plates, and rosettes) and riming degrees (Section 3.4). In Section 3.5, we combine findings from the previous sections and evaluate backscattering bias when applying both mass–size and SSRGA parameterizations.

2 | DATA AND METHODS

2.1 | Aggregation and riming model

To simulate rimed ice-crystal aggregates, we use the aggregation and riming model described in Leinonen *et al.* (2013), Leinonen and Szyrmer (2015), and Leinonen

and Moisseev (2015). For detailed descriptions of the algorithm, we refer the reader to these studies, consistent with Tridon *et al.* (2022) and Seifert *et al.* (2019). We chose to use model "B", where aggregation and riming occur sequentially, in order to differentiate between both processes and study effects of riming alone. First, N monomer crystals of a certain shape are generated from an exponential distribution. To span a wide range of particle sizes $D_{\max}$, where $D_{\max}$ is the maximum dimension of the particle, defined as the diameter of the smallest sphere circumscribing the particle, we generated aggregates with $N = 10, 20, 30, 40, 50, 100, 200, 300, 500, 700$ from exponential distributions with a mean $D_{\max}$ of 100 as well as 200 µm, as can commonly be found in nature (Pruppacher and Klett, 1997). The monomer crystals are composed of cubic volume elements with an edge length Δ, which is also the edge length of the cubic volume elements representing the frozen liquid water droplets. We chose Δ to be 20 µm, such that the liquid droplet size is similar to the one typically found in clouds (Lowenthal *et al.*, 2011). We performed the simulations for different monomer crystal shapes: columns, dendrites, needles, plates, and rosettes (while not allowing mixtures of them). The model simulates the ice and snow-particle aggregation by implementing a differential-sedimentation collection kernel and simple collision dynamics. Each monomer crystal is held only at a single orientation, but their orientations are randomized. The aggregates are aligned horizontally. Once aggregation is complete, the riming process begins, where the particles are exposed to a certain ELWP. The ELWP is the physical LWP along the particle's trajectory that would produce the given amount of riming if we assumed riming efficiency = 1. During riming, the particle's longest principal axis is reoriented perpendicular to the flow such that rime is evenly distributed on all sides.

For each N, mean monomer size and shape, we generated between 50 and 100 rimed aggregates, saving intermediate "evolution" steps to cover a wide range of riming levels. To keep the calculation duration within a reasonable time span, we chose a maximum ELWP of $2.0\,\mathrm{kg}\cdot\mathrm{m}^{-2}$.

In addition, the compaction algorithm by Seifert *et al.* (2019) for the aggregation and riming model is used to mimic the consolidation of the particle structure after ice-droplet collisions. The algorithm moves rime droplets slightly closer to the aggregate after contact. This allows us to generate denser rime, resulting in more accurate fall velocities of moderately and heavily rimed particles. We use their high-density rime (HDR) scenario with a rime density of $700\,\mathrm{kg}\cdot\mathrm{m}^{-3}$ (see Seifert *et al.*, 2019 for further information).

2.2 | Riming measure: Normalized rime mass M

In this study, the level of riming is quantified using the normalized rime mass M as proposed in Seifert *et al.* (2019). M is defined as the rime mass m_{rime} divided by the mass of the size-equivalent spherical graupel particle m_{g}:

$$M = \frac{m_{\mathrm{rime}}}{m_{\mathrm{g}}}, \tag{1}$$

where

$$m_{\mathrm{g}} = \frac{\pi}{6}\rho_{\mathrm{rime}} D_{\max}^3. \tag{2}$$

We chose M to quantify riming because it allows us to derive mass–size relations providing more realistic fall velocities (Tridon *et al.*, 2022), and this property may be used directly in evaluating the simulation of ice particles in atmospheric models, when using a bulk microphysics scheme like P3 (Morrison and Milbrandt, 2015). In the aggregation and riming algorithm we use, the amount of riming that an aggregate collects is controlled by the ELWP. We argue that M is a better measure to represent successive stages of riming than ELWP. The definition of M translates the asymptotic increase of m toward m_{g}, allowing Seifert *et al.* (2019) to show the self-similarity of the conversion of aggregates to graupel-like particles. ELWP is also difficult to determine from measurements and, while this may also be the case for M, the latter could in theory be determined in laboratory experiments if m_{rime} can be measured.

We save m_{rime} and $D_{\max}$ of each evolution step to calculate M. For large aggregates with $D_{\max} > 5$ mm, high M values above 0.3 are rarely reached because larger particles approach a spherical shape more slowly than smaller ones when exposed to the same amount of liquid water. It could be argued that this leads to a bias towards smaller particles for high M, but we wanted to keep the same conditions (i.e., ELWP) for all particles. With ELWP = $2.0\,\mathrm{kg}\cdot\mathrm{m}^{-2}$, we can simulate a large data set of particles that approach a graupel state. However, this limits the application of the proposed method such that it cannot be applied to deep convective clouds, where large graupel particles with diameters of several millineters to centimetres can form. Extending the framework to large graupel exceeds the scope of this study, but should be investigated in the future.

Figure 1 shows the evolution of two example aggregates riming. The top row displays an aggregate of 300 monomer needles taken from an exponential size distribution with mean diameters of 200 µm. When exposed to an ELWP of $2.0\,\mathrm{kg}\cdot\mathrm{m}^{-2}$, the particle reaches a maximum

FIGURE 1 Growth of two example aggregates by riming when exposed to an effective liquid water path (ELWP) of 2.0 kg · m^{-2}. Top: aggregate of 300 needles with mean monomer crystal sizes of 200 µm. Bottom: aggregate of 30 dendrites with mean monomer crystal sizes of 100 µm. The rimed aggregates consist of cubic volume elements with 20-µm width; the scale, shown in the first panel, is the same for images of each row. The normalized rime mass M at the different stages is included above each image. The larger needle aggregate does not reach higher M values than 0.224 with the chosen ELWP.

M of 0.224, representative of the extreme end for large aggregates that do not reach very high M values. The second row shows an aggregate of 30 dendrites with increasing amount of M, where the increase in M is depicted on an approximate logarithmic scale. Readers should note that the size scale included in the first column is different between the two rows. The example images show that we cover a wide range of ice and snow particle shapes and sizes ranging from unrimed through lightly rimed to heavily rimed, almost graupel-like particles.

Another important advantage of using M instead of ELWP as a measure of riming becomes apparent in Figure 1: the structures of particles with different sizes but the same M are similar to each other. While the large needle aggregate with $M = 0.214$ has about the same ELWP as the smaller dendrite aggregate with $M = 0.706$, its geometry is much more similar to the dendrite aggregate with $M = 0.211$.

2.3 | Scattering models

In order to measure properties of ice and snow particles by (microwave) remote sensing, one has to connect scattering to microphysical properties. The backscattering cross-section σ_b, the most important scattering property in radar measurements, is highly dependent on particle size, area, mass, and shape. Since these parameters are variable in nature, estimating scattering properties can lead to high uncertainties in radar retrievals of, for example, ice water content (IWC, Wood *et al.*, 2014). In this study, we calculated scattering properties for horizontally aligned ice and snow particles. Below, we give an overview of the methods for computing scattering that were used.

2.3.1 | Rayleigh–Gans approximation

RGA assumes that the individual parts of an arbitrarily shaped particle only interact with the incident wave and not with each other, which makes this method computationally cheap compared with, for example, DDA (Bohren and Huffman, 1983. For RGA to be applicable for the calculation of scattering properties of particles in the atmosphere, two conditions must be met. First, the complex refractive index m of the particle must be close to 1 (refractive index of air):

$$|m - 1| \ll 1. \tag{3}$$

Second, the scatterer should not be much larger than the wavelength along the propagation direction of the incident wave:

$$2kD|m - 1| \ll 1. \tag{4}$$

The first condition is generally met for nonrimed snow in the microwave regime. The second depends on the size D of the particle and the wavenumber $k = (2\pi)/\lambda$, where λ is the wavelength. Tyynelä *et al.* (2013) showed that these conditions can be relaxed for unrimed particles due to the lower refractive index of ice–air mixtures compared with pure ice. Riming, however, leads to higher densities, possibly violating the RGA requirements.

The backscattering cross-section σ_b of a particle can be calculated using RGA with

$$\sigma_b = \frac{9k^4}{4\pi} |K|^2 V^2 |f|^2, \tag{5}$$

where K is the dielectric factor and is usually calculated with the Clausius–Mossotti formula,

$$K = \frac{|m|^2 - 1}{|m|^2 + 2},$$

where m is the complex refractive index and we consider the particle to be composed by air with spherical ice inclusions. V is the volume and f is the so called Rayleigh–Gans form factor, given by

$$f_{\mathrm{RGA}} = \frac{1}{V}\int_V \exp\left[\mathrm{i}k\mathbf{R}(\hat{e}_z - \hat{e}_r)\right]\, d\mathbf{R}, \tag{6}$$

where $\mathbf{R}$ is the position within the particle, $\hat{e}_z$ is the unit vector in the direction of the incident wave, and $\hat{e}_r$ the unit vector in the direction of the scattered wave. f_{RGA} accounts for the cumulative destructive interference among the waves scattered by the various parts of the particle. If one assumes small volume elements, each with volume V_j, the term can be discretized into

$$f_{\mathrm{RGA}} = \left(\sum_{j=1}^{N} V_j\right)^{-1} \sum_{j=1}^{N} V_j \exp\left[\mathrm{i}k\mathbf{R}\,(\hat{e}_z - \hat{e}_r)\right]. \tag{7}$$

In the case of backscattering, the direction of the incident wave vector is exactly opposite to the direction of the scattered wave vector $\hat{e}_z = -\hat{e}_r$. Assuming volume elements with equal sizes, this leads to a simplification of the form factor to

$$f_{\mathrm{RGA}} = \sum_{j=1}^{N} \exp\left(-2\mathrm{i}kz_j\right), \tag{8}$$

where z_j are the z coordinates of the volume elements. Nonspherical scatterers, as is the case for ice and snow particles, require adjustments to RGA because of their different polarizability. In the case of aggregates of randomly oriented nonspherical monomer ice crystals, the total polarizability is isotropic and the nonsphericity of the monomers can be accounted for by adopting a modified K factor. This has been shown by Hogan *et al.* (2017), who called the modified factor K_{NS}. As discussed in Leinonen *et al.* (2018), K_{NS} cannot be calculated directly for the aggregates generated by the aggregation and riming model used in this study, due to riming altering the shape of the monomer crystals. However, K_{NS} can be estimated by comparing the normalized absorption cross-section C_{abs}/V calculated by RGA and DDA for unrimed particles. Following their approach, we calculated C_{abs}/V for 35.6 and 94.0 GHz for a subset of particles and reached the best agreement with $|K_{\mathrm{NS}}|^2 = 0.23$ for both frequencies, close to their value of 0.21 and higher than the dielectric factor of ice $|K|^2 = 0.18$. Our value corresponds to plates of aspect ratio 0.2 in the K_{NS} formula in Westbrook (2014).

2.3.2 | Self-similar Rayleigh–Gans approximation

Hogan and Westbrook (2014) developed an analytic expression for the RGA form factor by exploiting the fractal nature of ice and snow particles. They provide a way to calculate the *average* σ_{b} for an *ensemble* of (unrimed) aggregates in the microwave frequency range. This forms the basis for SSRGA, which was further expanded by Hogan *et al.* (2017). SSRGA is described by five dimensionless parameters: $\alpha_{\mathrm{e}}, \kappa, \beta, \gamma, \zeta_1$, which we refer to as "the SSRGA parameters". The SSRGA form factor in the backscattering direction can be calculated by

$$\begin{aligned} f_{\mathrm{SSRGA}}(x) = \frac{\pi^2}{4}\Bigg[&\cos^2(x)\left\{\left(1+\frac{\kappa}{3}\right)\left(\frac{1}{2x+\pi}-\frac{1}{2x-\pi}\right)\right. \\ &\left.-\kappa\left(\frac{1}{2x+3\pi}-\frac{1}{2x-3\pi}\right)\right\}^2 \\ &+\beta\sin^2(x)\sum_{j=1}^{N_{\mathrm{terms}}}\zeta_j(2j)^{-\gamma}\left\{\left(\frac{1}{2x+2\pi j}\right)^2\right. \\ &\left.+\left(\frac{1}{2x-2\pi j}\right)^2\right\}\Bigg]. \end{aligned} \tag{9}$$

Here, x is the size parameter $x = kD = k\alpha_{\mathrm{e}}D_{\mathrm{max}}$, where D is the particle size in the direction of the propagating light. The effective aspect ratio is given by $\alpha_{\mathrm{e}} = D/D_{\mathrm{max}}$. If ice and snow particles are aligned horizontally and the radar is pointing vertically, α_{e} is the same as the aspect ratio α of the particles. κ is called the kurtosis parameter and is a measure of the mean mass distribution of the particle along the propagation direction (positive values indicate more mass in the centre, negative values a homogeneous distribution of mass). β and γ are the power-law prefactor and exponent describing the mass fluctuations around the mean mass distribution. ζ_1 is a correction term for the power spectrum of the smallest wavenumber. The correction is needed because the smallest wavenumber often deviates from the power-law fit; all other ζ_j values are 1.

In this study, we used the snowScatt tool by Ori *et al.* (2021) to perform SSRGA parameter fits for the generated rimed aggregates, grouped by M and D_{max}. snowScatt follows the method described in Hogan *et al.* (2017).

As stated by Hogan *et al.* (2017), the accuracy of SSRGA is limited by the realism of the simulated particles that the SSRGA parameter was calculated for. It is therefore important to be cautious when using values proposed in the literature and evaluate whether the corresponding modelled particles represent the studied ice-particle population well.

2.3.3 | Discrete dipole approximation

To evaluate the applicability of RGA for rimed aggregates, we used DDA (Draine and Flatau, 1994) as a reference method. With DDA the scatterer is divided into small homogeneous volume elements, which each act as a dipole. Therefore, the complete interactions between the volume elements are modelled. DDA provides accurate results as long as the volume elements are sufficiently small compared with the wavelength. Assuming cubical dipoles, the generally accepted threshold is $d < \lambda/(10|m|)$, where d is the maximum span of the dipole (Yurkin *et al.*, 2007). This criterion is met for all our calculations. A similar validity criterion is given by $kd|m| < A$, where A should be 0.5 according to Zubko *et al.* (2010). For us, A is largest in the W band with $A = 0.070$.

We used the C software package ADDA, developed by Yurkin and Hoekstra (2011) to calculate the amplitude matrix $\mathbf{S}$:

$$\mathbf{S} = \begin{bmatrix} S_2 & S_3 \\ S_4 & S_1 \end{bmatrix}. \tag{10}$$

σ_b can be calculated from $\mathbf{S}$ with

$$\sigma_b = \frac{2\pi}{k^2}\left(|S_1(\pi,0)|^2 + |S_2(\pi,0)|^2\right). \tag{11}$$

We opted to calculate backscattering cross-sections σ_b at 35.6 GHz (Ka band) as well as 94.0 GHz for horizontally aligned ice and snow particles. We took the complex refractive indices of ice at each frequency from the tables of Warren and Brandt (2008), where a temperature of 266 K is assumed.

2.4 | Parameterization of SSRGA parameters by M

Riming changes the structure of aggregates, which impacts their scattering properties. Therefore, literature values of SSRGA parameters found for unrimed particles do not necessarily hold for rimed aggregates, possibly leading to large uncertainties in, for example, radar retrievals. In the following, we will develop a "riming-dependent parameterization" of the SSRGA parameter.

The SSRGA parameters we calculated using snowScatt for our rimed aggregates do not show a simple linear, power-law, or polynomial dependence on M. We evaluated fitting each parameter with the aforementioned function types, but were not able to derive a function of each SSRGA parameter depending on M that obtained better results than by the following method. We performed linear discriminant analysis (LDA) to reduce the dimensions from five parameters to two (using two instead of one parameter allows us to have less information loss when inverting the problem). LDA is a statistical method to find a linear combination of features that separates two or more classes based on Fisher's linear discriminant. It is commonly used to reduce the dimensionality of a problem (McLachlan, 2005). We also evaluated using principal component analysis (PCA) to reduce dimensionality, but found LDA to be more convenient for this application. We used the Python software *sklearn* (Pedregosa *et al.*, 2011) with α_e, κ, β, γ, ζ_1 as features and M in form of string class names.

Figure 2 shows the resulting two parameters, here simply referred to as x_{LDA} and y_{LDA}, with their M values colour-coded. One point in the scatter plot does not represent one particle but one size bin for a certain M class and monomer shape, resulting from the SSRGA parameter fit. There are a minimum of 30 particles per size bin, with an average number of 1000–4000 rimed aggregates per bin. The aggregates can be the same particle, but an earlier or later evolution step, as long as they fall into the same M bin. Mean values of the reduced dimension x_{LDA} for the different M groups depend on M via a power

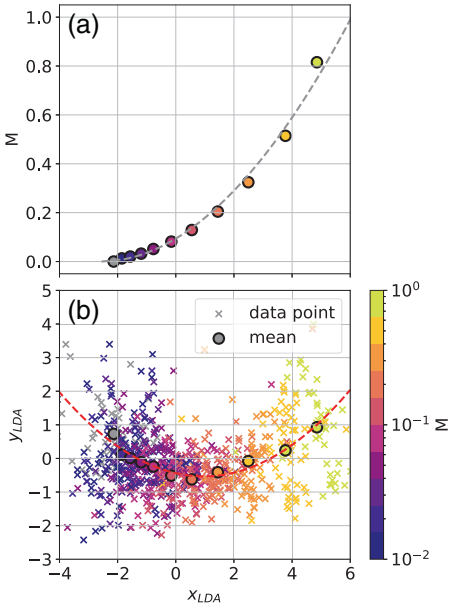

FIGURE 2 Results of the dimensionality reduction performed by linear discriminant analysis (LDA) to derive two variables x_{LDA} and y_{LDA} from the five SSRGA parameters and their relation to the normalized rime mass M: (a) mean x_{LDA} versus M including a power-law fit as a grey dashed line, (b) individual data points shown as crosses colour-coded by their M bin (grey indicates $M = 0$) and mean values for each M bin depicted as circles of the corresponding colour. The red dashed line shows a quadratic fit to parameterize mean y_{LDA} through mean x_{LDA} values.

law (Figure 2a). In addition, mean y_{LDA} can be expressed through mean x_{LDA} with a quadratic function (Figure 2b). Therefore, we applied two fits and obtained expressions for the two reduced dimensions from M. LDA cannot be inverted directly, since there must be a loss in information when going from a higher to a lower dimension. However, using the pseudo inverse matrix of the LDA, we can reconstruct the SSRGA parameter from x_{LDA} and y_{LDA} sufficiently well for our purposes. Thus, the resulting function of each SSRGA parameter is a composition of a linear, a quadratic and a power-law function and has the following form:

$$\text{SSRGA parameter} = p_1\, M^{2p_0} + p_2\, M^{p_0} + p_3, \tag{12}$$

where p_i are calculated from the fits.

Because the resulting function of each parameter only depends on M, we evaluated fitting each SSRGA parameter separately to Equation 12. However, we could not achieve lower biases than with the p_i calculated via the LDA method presented above. We are aware that, by fitting an averaged SSRGA parameter, we inevitably move away from the physical meaning of the SSRGA parameter. Our goal is not a physical consistent description of SSRGA parameters but a realistic estimation of bulk backscattering cross-sections. Although this method is rather abstract, the resulting parameterizations of the SSRGA parameter allow us to estimate backscattering properties of aggregates as a function of their degree of riming.

We also evaluated the inclusion of the size $D_{\max}$ as additional information, but this did not lead to improvements. Further, we performed the SSRGA parameter fit with snowScatt for linear as well as logarithmic size bins, the former with a bin size of 100 as well as 200 µm, the latter for 20 and 30 logarithmic bins each, and applied this method to all configurations to see how robust our proposed SSRGA parameter functions are. The resulting p_i values are the same, within 20% (maximum discrepancy) of the presented values for different $D_{\max}$ binning, with an average difference of below 1%. Therefore we will present only the results for the 20 logarithmic size bins.

We obtain the following parameterizations of the SSRGA parameter depending only on M:

$$\alpha_{\mathrm{e}} = 0.160\, M^{1.028} + 0.187\, M^{0.514} + 0.575, \tag{13}$$

$$\kappa = -0.100\, M^{1.028} + 0.068\, M^{0.514} + 0.194 \approx 0.19, \tag{14}$$

$$\gamma = -1.27\, M^{1.028} + 1.79\, M^{0.514} + 2.76, \tag{15}$$

$$\beta = 4.06\, M^{1.028} - 7.47\, M^{0.514} + 5.42, \tag{16}$$

$$\zeta_1 = 0.127\, M^{1.028} - 0.091\, M^{0.514} + 0.067 \approx 0.06. \tag{17}$$

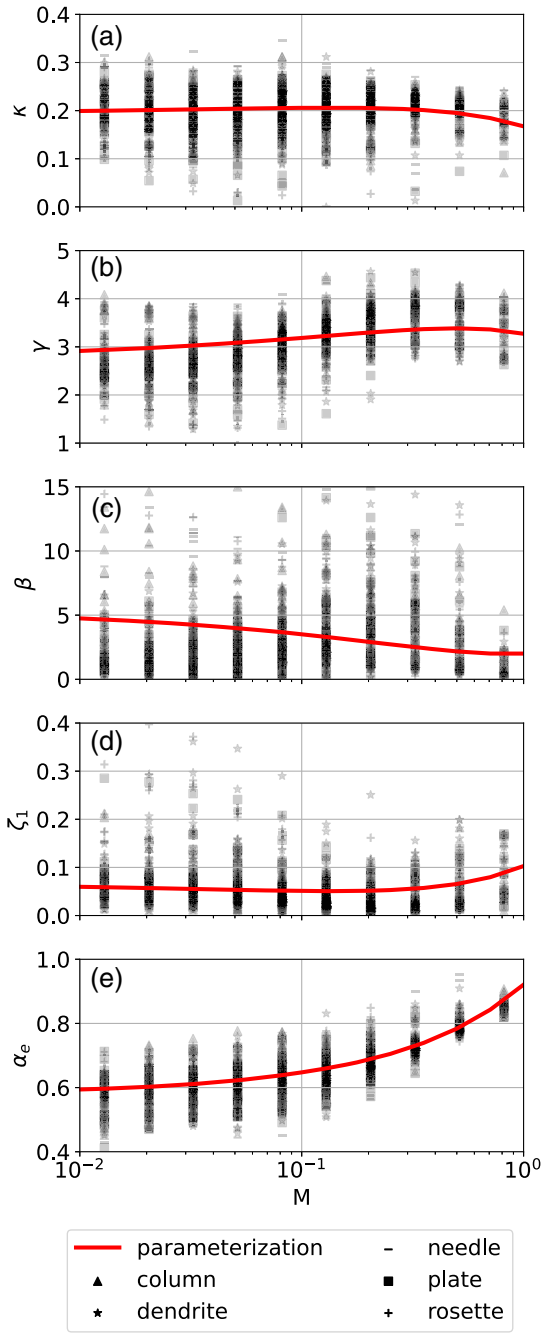

FIGURE 3 Results of the SSRGA parameter calculations obtained by snowScatt versus the binned normalized rime mass M. The markers show the individual results for 200-µm linear size bins. The marker type indicates the different monomer types, the opacity is reduced to show the density of the results. The derived functions to approximate the SSRGA parameters by M are shown as red lines. [Colour figure can be viewed at wileyonlinelibrary.com]

Figure 3 shows the calculated SSRGA parameters α_{e}, κ, β, γ, ζ_1 versus M, where one point represents one size bin. The different monomer shapes are shown as different markers and their opacity is reduced in order to illustrate where the majority of data points fall. Equations 13–17

are included as red lines, following the shape of the density concentration of the corresponding SSRGA parameter well. The parameterized κ and ζ_1 values are close to constant for all but the highest M bin. We use the empirical function instead of the approximated constant values in our further analysis, because our simulated rimed aggregates do contain particles with high M. When one wants to apply these parameterizations to ice-particle populations with a low likelihood of very heavily rimed particles, using constant κ and ζ_1 values will not lead to a significant increase in uncertainty. For β, the riming-dependent parameterization shows the largest discrepancy to the area of highest density of snowScatt derived values. However, the function falls well within the range of snowScatt β values, which suggests values as high as 75 (not shown here). The derived parametrization shows a reduction of β with the increase of M. This indicates a general tendency of the snowflake mass distributions to reduce their deviations with respect to the mean shape. Additionally, the increase of the γ parameter shows that this reduction affects the smallest scales first, which is consistent with the riming model adopted, which uniformly adds small ice volumes to the snowflake (Leinonen and Szyrmer, 2015). The value of κ tends to become lower for larger M, indicating a tendency to make the mass distribution more even (less peaked in the centre). α_e shows the highest correlation with M. Increasing α_e with increasing M means particles are more spherical the more they are rimed. This behaviour is expected, because heavily rimed particles approach a spherical shape with $\alpha_e = \alpha = 1$, as can be seen in Figure 1.

2.5 | Parameterization of mass– and area–size relations by M

Due to the highly variable geometry of ice and snow particles in nature, it is common practice to relate their particle size D_{max} to particle mass m and cross-sectional area A by power laws:

$$m = a_m \, D_{max}^{b_m}, \tag{18}$$

$$A = a_A \, D_{max}^{b_A}. \tag{19}$$

We refer to Equation 18 as the mass–size relation and Equation 19 as the area–size relation, with a_m and b_m being the mass–size and a_A and b_A the area–size parameter. Typically, the parameters of the mass– and area–sizes vary strongly with particle type (Mitchell, 1996). We present mass–size and area–size parameter results a_m, b_m and a_A, b_A for aggregates of the monomer shapes and riming degrees studied in Section 3.4.

3 | RESULTS AND DISCUSSION

In the following sections, we present backscattering cross-section σ_b bias calculations evaluating the applicability of RGA compared with DDA as a reference method for a subset of particles in Section 3.1. Further, we show the performance of SSRGA versus DDA using the riming-dependent parameterization for the same subset in Section 3.2. These are necessary steps to provide evidence that SSRGA can be applied to rimed particles (with some caution) when quantifying riming by M. In Section 3.3, we compare the use of the riming-dependent parameterization against SSRGA values and parmeterizations found in the literature for calculating the SSRGA parameters. We present results both for individual particles (Section 3.3.1) and for particles following size distributions (Section 3.3.2). In addition, we present mass–size and area–size relations dependent on M in Section 3.4. Finally, we evaluate the performance of combining mass–size and riming-dependent parameterization of SSRGA in Section 3.5. Calculations of the extinction cross-section, which is defined as the sum of absorption and scattering cross-sections, are discussed in the Supporting Information (Figures S1–S8).

3.1 | Bias of RGA versus DDA

This section presents the bias in σ_b calculated by RGA and DDA to evaluate the size parameter x and normalized rime mass M up to which the RGA method (and therefore SSRGA) provides reasonable accuracy in backscattering cross-section σ_b compared with DDA. DDA calculations of σ_b are described in Section 2.3.3. We calculated the bias in units of relative difference (in percent) as well as dB, which is commonly used for cloud radars in meteorology, for frequencies of 35.6 and 94.0 GHz:

$$\text{bias}(\%) = 100 \, \frac{\sigma_{b,\,RGA} - \sigma_{b,\,DDA}}{\sigma_{b,\,DDA}}, \tag{20}$$

$$\text{bias}(\text{dB}) = 10 \, \log_{10}\left(\frac{\sigma_{b,\,RGA}}{\sigma_{b,\,DDA}}\right). \tag{21}$$

Here it must be noted that relative differences in percent and dB have different meanings. For example, ±3 dB means a bias of a factor of 2 and therefore relative differences of +100% for +3 dB and −50% for −3 dB. By definition, positive relative differences can, in principle, become infinitely large, while negative relative differences can be minimally −100%.

Since DDA calculations are computationally expensive, we performed the bias calculations for a subset of

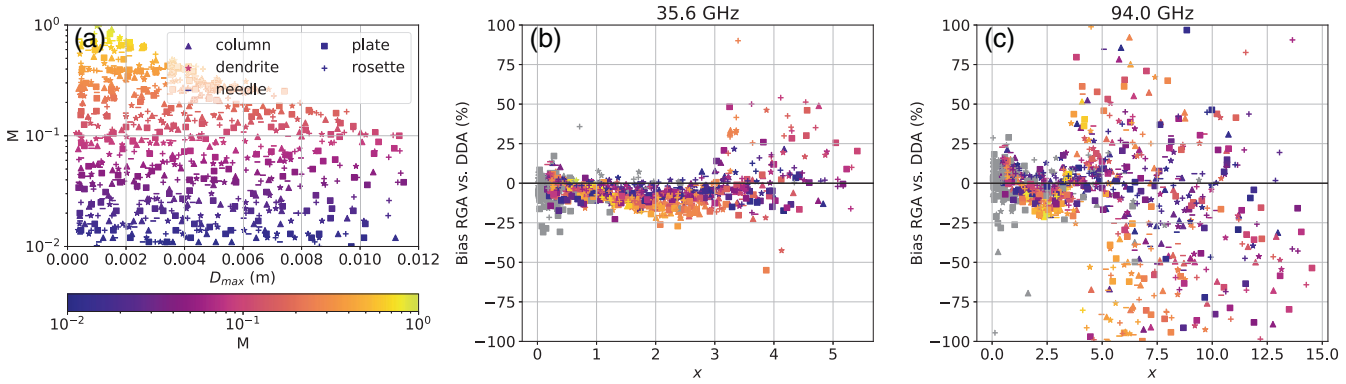

FIGURE 4 The RGA versus DDA backscattering cross-section bias for rimed aggregates of different sizes: (a) the selection of aggregates for which the RGA versus DDA calculations were done, size $D_{\max}$ is plotted against normalized rime mass M. The marker colour indicates M, the shape the monomer crystal type. The other plots show the bias results in percent for (b) 35.6 GHz and (c) 94.0 GHz. Note the different y scales. Vertical grey dashed lines show the wavelength. Unrimed particles ($M = 0$; not depicted in panel a) are included in grey.

rimed and unrimed aggregates that are representative of our full data set in terms of size and M values. The sample includes 205 aggregates composed by columns, 216 by dendrites, 193 by needles, 236 by plates, and 223 by rosettes, of which respectively 43, 47, 48, 59, and 43 are unrimed.

The resulting biases for 35.6 GHz (Figure 4b) and 94.0 GHz (Figure 4c) are shown together with M of all particles in Figure 4. The selected particles cover a wide range of sizes and riming degrees, as can be seen in Figure 4a. Similar to Tyynelä *et al.* (2013), we find an underestimation of RGA compared with DDA that we could not correct fully by using the modified K_{NS}. However, this underestimation, of on average less than 5% or 1 dB regardless of wavelength, is far smaller than the 4.6 dB found by Tyynelä *et al.* (2013) and small compared with typical radar measurement uncertainties: for example, Myagkov *et al.* (2020) show uncertainties from calibration alone to be ±0.9 dB for W-band radars. As long as the particle size $D_{\max}$ is smaller than the wavelength, RGA performs sufficiently well, with 90% of data having biases in the range −17.0% to 5.9% or −0.8 to +0.3 dB and −17.8% to 25.1% or −0.9 to +1.0 dB in the Ka and W bands, respectively. For $x > \pi$, meaning $D_{\max} > \lambda$, the bias of individual particles is large, especially in the W band, ranging down to −29 dB (meaning RGA underestimating DDA), corresponding to close to −100%. However, when averaging particles with constant M over all particle sizes, the absolute (logarithmic) mean bias is below 13% or 0.5 dB in the Ka band (with RGA values generally lower than DDA) for all M bins and in the W band for $M < 0.4$. For the W-band and $M > 0.4$, the mean bias is +30.1% or −1.2 dB, where the large relative bias is due to outliers, to which the logarithmic dB scale is less sensitive (median bias is −10.1%; not shown).

3.2 | Bias of the SSRGA riming-dependent parameterization versus DDA

Previous studies showed that SSRGA approximates DDA and RGA results with good accuracy for both unrimed (Hogan *et al.*, 2017; Ori *et al.*, 2021) and rimed particles (Leinonen *et al.*, 2018; Ori *et al.*, 2021). As can be seen in Figure 5, this also holds for particles of any M when using the riming-dependent parameterization to calculate the SSRGA parameter. We show the DDA backscattering cross-sections σ_{b} calculated for the selected individual particles from Figure 4 as well as the running average of SSRGA σ_{b} using the exact particle masses. Some individual particles deviate significantly from the DDA results, with SSRGA–DDA biases ranging from −91 to 5.0 $\times 10^4$% or −10 to 19 and −91 to 1.6 $\times 10^5$% or −11 to 32 dB in the Ka and W bands for the extreme cases. In general, SSRGA fits DDA well, with mean biases over x of particles in a given M bin in the range −29.1 to −4.5% or −1.11 to −0.37 dB for the Ka band and −20.3 to −18.1% or −0.54 to 1.57 dB in the W band for $D_{\max} < \lambda$. Especially for $D_{\max} > \lambda$, σ_{b} calculated by DDA for different M bins shows a larger spread than that from SSRGA, spanning three size orders compared with one for slightly rimed particles ($0 < M < 0.1$) in the Ka band (W band: four and three size orders, respectively). More heavily rimed ($M > 0.1$) particles with $D_{\max} > \lambda$ range from $\sigma_{\mathrm{b}} \approx 10^{-7}$ to 10^{-6} m^2 for both RGA and SSRGA in the Ka band (W band: approx. 10^{-10} to 10^5 for DDA and 10^{-7} to 10^{-6} m^2 for SSRGA).

SSRGA using the riming-dependent parameterization can therefore be applied for rimed aggregates and sizes $D_{\max} < \lambda$. For $D_{\max} > \lambda$, the underlying RGA provides reasonably accurate results when averaged over the particle

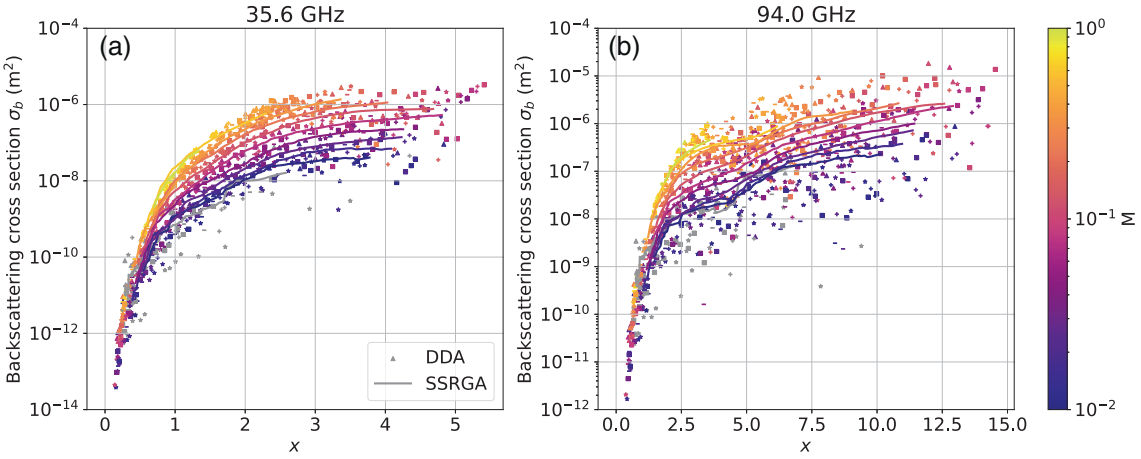

FIGURE 5 SSRGA and DDA backscattering cross-sections for rimed aggregates of different sizes for (a) 35.6 GHz and (b) 94.0 GHz, note the different y scales. Vertical grey dashed lines show the wavelength. Unrimed particles ($M = 0$) are included in grey. Individual markers represent DDA, while lines show the running average of the SSRGA results. The SSRGA calculations used the riming-dependent parameterization and the exact particle masses.

size spectrum, with biases of around 11% or 0.5 dB compared with DDA for all riming levels in the Ka band as well as particles with $M < 0.4$ in the W band (not shown). SSRGA can thus be used for radar retrievals, where one usually observes particles of different size ranges. However, results should be treated with caution for $D_{max} > \lambda$, especially when dealing with very high degrees of riming.

3.3 | Bias of parameterized versus fixed SSRGA parameters

The previous section demonstrated the accuracy of RGA in reference to DDA as well as SSRGA using the riming-dependent parameterization in reference to DDA for a small, selected sample of particles. In the following, the performance of the riming-dependent parameterization, taking the SSRGA parameter calculated directly for a group of particles with similar size and M values with snowScatt as a reference, will be analysed by the σ_b bias in dB. The snowScatt fit results for α_e, κ, β, γ, ζ_1 can be assumed to be reasonably accurate for the size and M range, where RGA performs well compared with DDA (Ori *et al.*, 2021). As shown in Section 3.1 for individual particles, this is the case for sizes smaller than the wavelength. When considering an ensemble of particles, RGA and therefore SSRGA provides results with mean biases within 11% or 1.0 dB, except for M values exceeding 0.4 in the W band, where mean biases reach up to +30% due to outliers (median = −11.2%) or −1.2 dB even when particles larger than the wavelength are included.

Here, we further compare the biases calculated using the riming-dependent parameterization of the SSRGA parameter with those obtained using literature values.

TABLE 1 Literature values for the five SSRGA parameters.

Parameter	HW14—Westbrook et al.	H17—Westbrook et al.	H17—Nowell et al.
α_e	0.6	0.83	0.82
κ	0.19	0.09	$0.16D_{max}^{0.44}$
β	0.23	$0.86D_{max}^{-0.3}$	$0.15D_{max}^{0.64}$
γ	5/3	2	7/3
ζ_1	1	0.28	$0.22D_{max}^{-0.44}$

Note: D_{max} is in millimetres and the H17 fits are limited to 1–10 mm.

Included are the values calculated by Hogan and Westbrook (2014) for the Westbrook *et al.* (2004) aggregate model (from here on denoted as HW14—Westbrook) as well as the fit results from Hogan *et al.* (2017) for the same Westbrook *et al.* (2004) aggregate model (H17—Westbrook) and the Nowell *et al.* (2013) model (H17—Nowell). All SSRGA parameters from these studies are summarized in Table 1. We evaluate biases in dB because the focus of this study is the application to radar observations and radar forward modelling.

Discrepancies between these literature values and the riming-dependent parameterization are expected, since they were derived for different particle models. The literature values are commonly used in radar retrievals, as for example in Maahn and Löhnert (2017), who had to limit their analysis to nonrimed particles. Our comparison shows that using them can lead to high uncertainties, especially when applied to rimed particles, which likely behave more similarly in nature to our modelled particles that consider riming. The aim of this study is also to highlight the need for am SSRGA parameterization designed for the

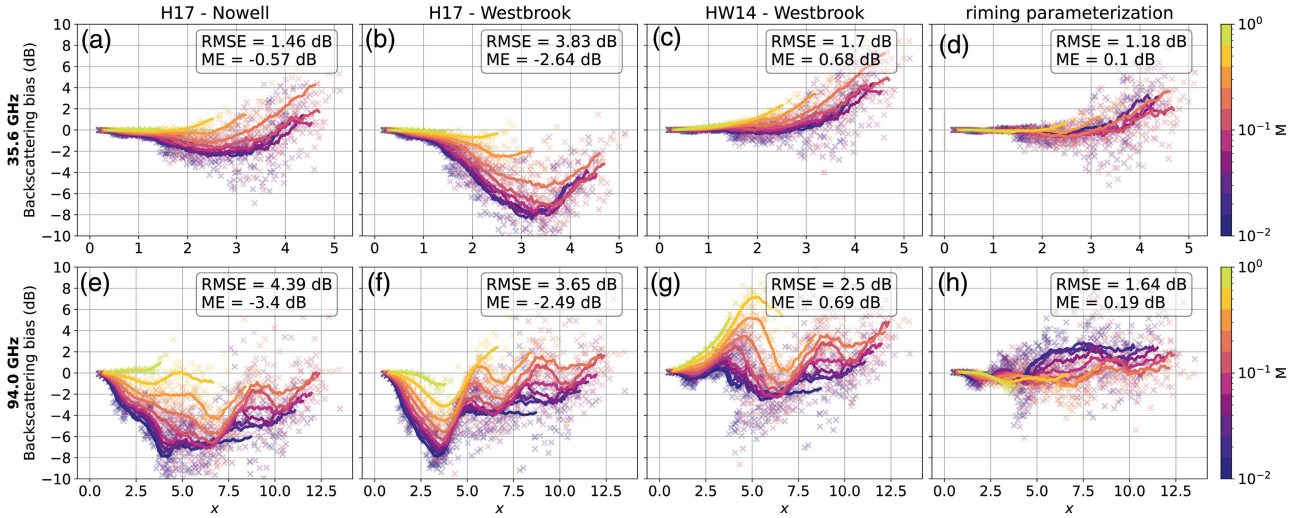

FIGURE 6 Backscattering cross-section bias in dB using fixed or parameterized SSRGA parameter in reference to calculated values versus size parameter x for (a)–(d) 35.6 GHz and (e)–(h) 94.0 GHz. The cross markers show results for 200-μm linear size bins. Their colour indicates the normalized rime mass M (consistent with Figure 4). The coloured curves show the running mean bias for each M bin. (a)–(c) and (e)–(g) show the results for SSRGA values proposed in the literature (see Table 1), (d) and (h) show the riming-dependent parameterization (M parameterization). The root-mean-square error RMSE and mean error ME of the biases are shown in each panel on the top right.

specific ice and snow particle types involved in the simulation. The riming-dependent parameterization can help in this sense by providing a useful functional form that generates SSRGA parameters for a wide range of snow types, specifically rimed aggregates at diverse stages of riming.

3.3.1 | Individual particles

Figure 6 shows the bias of σ_b using our proposed SSRGA parameterization as well as literature values (Table 1) compared with the reference values calculated with snowScatt for 35.6 (Figure 6a–d) as well as 94.0 GHz (Figure 6e–h). One point represents a size bin, an M bin, and a particle type, where the snowScatt fits were performed. It therefore represents an average particle of that size and M. We chose to show the results of the linear size binning with a bin size of 200 μm to show a larger set of data points compared with the logarithmic bins. x is plotted on a linear scale to focus on larger sizes, where biases are expected to be bigger than for small particles. In addition, running averages over 20 data points for the M bins are included as coloured lines. The averaged values for unrimed particles are not visible in the figure for two reasons: first, the unrimed particles are generally smaller, so the running averages are only performed up to about 2 mm, and, second, they follow very closely those for the lowest M bin (dark blue).

For both wavelengths, the average bias using the riming-dependent parameterization is much smaller than using literature values, resulting in root-mean-square errors of 1.15 and 1.64 dB and mean errors of 0.10 and 0.19 dB in the Ka and W bands, respectively (literature RMSE = 1.42–3.8/2.5–4.39 dB for Ka/W band; ME = −2.6–0.65/−3.4–0.69 dB). Biases for individual particles scatter significantly at sizes larger than the wavelength regardless of the chosen SSRGA parameter method, ranging from −5 to +6 dB for the riming-dependent parameterization. The riming-dependent parameterization performs especially well for all M levels for sizes smaller than the wavelength with average absolute biases below 2dB. Using the literature values, the bias for unrimed and very lightly rimed particles is only mostly below 2 dB for the HW14—Westbrook et al. parameters, even though all literature SSRGA parameter were derived for unrimed particles. The use of literature SSRGA parameters derived for more "open" aggregate structures implies that the aggregate mass distribution decorrelates at small scales, while in reality, rimed particles are more homogeneous. The higher autocorrelation of the mass distribution determines a reduced destructive interference of the scattered waves, hence an augmented backscattering cross-section with respect to the literature SSRGA models.

3.3.2 | Applying a size distribution

When measuring ice cloud or snowfall properties by microwave remote sensing, the scattering properties of a single ice particle are less relevant than those of an ensemble of particles. Commonly, particle size distributions

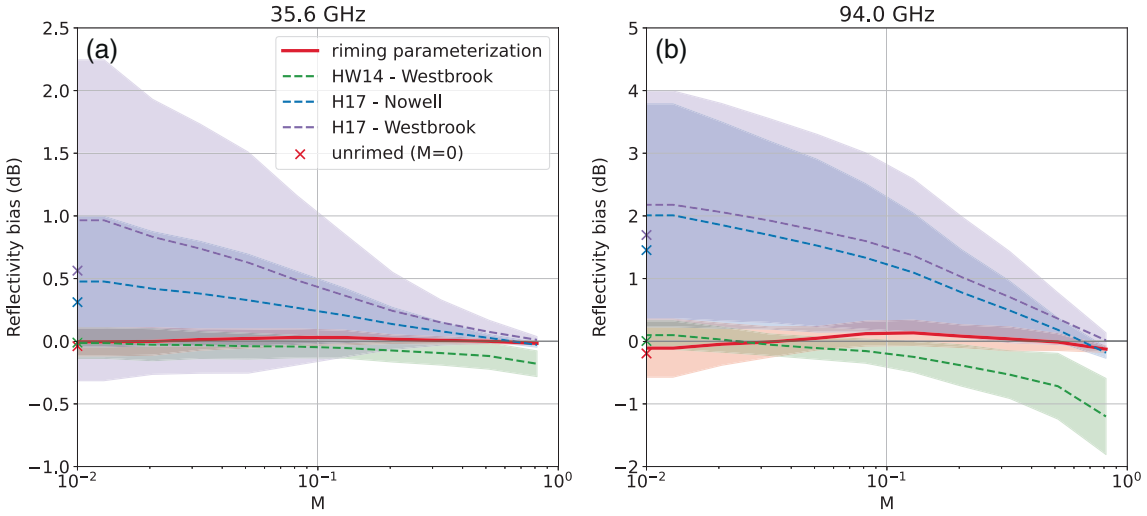

FIGURE 7 Radar reflectivity bias in dB using parameterized SSRGA parameter in reference to parameter values obtained by snowScatt for a sample of exponential size distributions versus normalized rime mass M for (a) 35.6 GHz (b) and 94.0 GHz. Coloured dashed lines show the mean results for the literature SSRGA parameter (Table 1) whereas the red solid line shows the riming-dependent parameterization. Standard deviations are depicted as shaded areas of the corresponding colour. Bias values for unrimed particles ($M = 0$) are shown as cross markers on the y-axis.

(PSDs) are used to represent the ice and snow particle populations. Various studies have shown that PSDs in ice clouds can follow exponential (e.g., Field *et al.*, 2005), gamma (e.g., Maahn *et al.*, 2015), or lognormal functions (e.g., Tian *et al.*, 2010). There is so far no consensus regarding the best way to parameterize an ice-particle size distribution; we reduce complexity and use the exponential size distribution, a simplification of the gamma distribution. It is expressed by

$$N(D) = N_0 \ \exp(-\Lambda D), \tag{22}$$

where N is the number concentration in m^{-3} of particles of size D in m, the intercept parameter N_0 (in m^{-3}) describes the overall scaling, and the slope parameter Λ controls the shape. Field *et al.* (2005) presented a way to derive N_0 from ambient temperature T alone. They obtained their findings via aircraft measurements of stratiform ice clouds around the British Isles. N_0 can be expressed as

$$N_0 = 7.6275\ 10^6 \ \exp(-0.107T). \tag{23}$$

The ambient temperature T is in °C and Λ can be obtained from the total number of particles N_{tot} with $\Lambda = N_0/N_{tot}$. The latter expression is obtained from the definition of N_{tot} by integrating Equation 22 over the full size range from 0 to $+\infty$ and solving for Λ.

Figure 7 shows the average bias of the equivalent radar reflectivity Z_e for 35.6 (Figure 7a) and 94.0 GHz (Figure 7b) using our SSRGA parameterization as well as the literature values from Table 1, in reference to the snowScatt calculated SSRGA parameters for exponential PSDs calculated by Equations 22 and 23. We use snowScatt to calculate Z_e. For each M bin, we calculated PSDs for temperatures from −30 to −2 °C in 2-K steps. N_{tot} was varied between 10^3 and 10^5 m^{-3} and all PSDs resulting in unrealistic Z_e values ($Z_e < -40$ and $Z_e > 30$ dBZ) were excluded. The plot shows the mean bias in dB for each M as dashed lines for the literature values and as a solid red line for the riming-dependent parameterization (M parameterization). The corresponding standard deviations from the various size distributions are included as shaded areas. The riming-dependent parameterization performs well compared with the literature SSRGA values, resulting in small biases below 1.0 dB in the W band over all degrees of riming. Biases in the Ka band are even smaller, with the mean falling right along the 0 line. Because large particles do not reach as high an M as small ones, size distributions for larger M are cut off at certain D_{max}. Particles in the (second/third/fourth) highest M bin have maximum sizes of about 2 mm (4/6/10). This likely leads to the decrease of standard deviations with increasing M for all parameterizations.

3.4 | Mass– and area–size relations

Mass– and area–size relations are commonly parameterized by power laws. For the exponent of the mass–size relation, b_m, a wide range of values derived from measurements and model studies exist in the literature, with b_m ranging from 1.7 (Locatelli and Hobbs, 1974) to 3.0

(Mitchell, 1996). Parameters proposed by Brown and Francis (1995) are commonly used (in SI: $a_m = 0.0121$, $b_m = 1.9$) in retrievals and models. According to findings from Westbrook *et al.* (2004) based on aggregation theory, b_m should approach values close to 2 for large unrimed aggregates. According to the fill-in model, liquid water droplets fill the "gaps" in the structure of the aggregate, leading to an increase of mass m but not size D_{max}. Model studies have shown that the fill-in model is only realistic in the very early stages of riming (Leinonen and Szyrmer, 2015; Seifert *et al.*, 2019). Soon in the riming process, rime starts to accumulate on the outside of the ice particle, increasing D_{max}. This leads to an increase of b_m values, which is in disagreement with the fill-in model. Since ice and snow particles tend to orient themselves perpendicular to the flow and rime is mainly collected on the bottom of the particle when falling through layers of supercooled liquid, the particles become more spherical with increasing levels of riming. During this process, both a_m and b_m increase further. In the extreme scenario, when the particle reaches a spherical graupel stage, b_m should approach 3. Assuming ice-particle size independent collection efficiencies of liquid droplets, smaller ice particles reach the graupel stage faster than larger ones.

A similar behaviour can be assumed for the cross-sectional area. With increasing amounts of riming, the area approaches a circle where b_A approaches 2. Mitchell (1996) found that values for b_A derived in various laboratory and in situ studies range from 1.4 to 2.0. Monomer shape is expected to play a less important role in the mass and area–size parameters for aggregates that are sufficiently large compared with the size of the monomer crystals from which they are composed. Needles, for example, usually have a much smaller cross-sectional area and mass than dendrites of the same D_{max}.

Figure 8 shows the evolution of particle mass m (Figure 8a) and particle cross-sectional area A (Figure 8b) versus the size D_{max} during the riming process. As an example, only aggregates of needles are shown; plots for the other monomer types can be found in the Supporting Information (Figures S9–S12). The normalized rime mass M is colour-coded and power-law fits over 10 logarithmic M bins from 10^{-2} to 10^{0} are shown. Unrimed aggregates are coloured grey. While the fits were performed for all particles and evolution stages falling in the corresponding M bin, one out of 50 particles is plotted. The resulting colour gradient in the figure shows a clear relation between the mass and area–size parameters and M. Mass and area–size parameters are larger for more heavily rimed particles. Riming impacts the mass–size relation to a greater degree than the area–size relation. Unrimed needles have $b_m = 2.06$, close to the theoretical values of 2. For the highest two M bins ($M > 0.5$), $b_m \approx 3.0$ holds. b_A also increases with

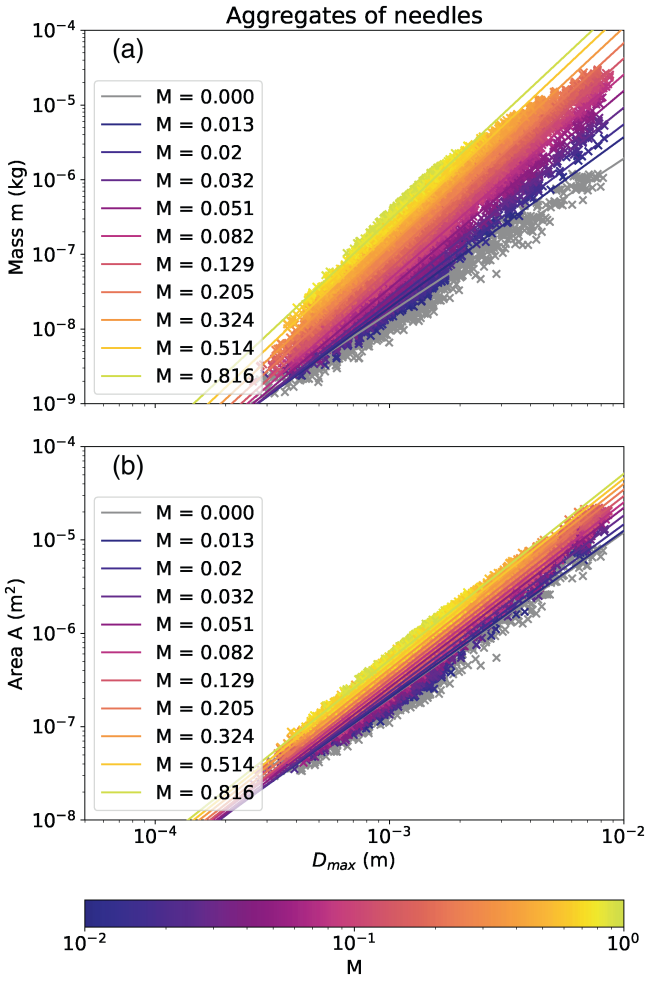

FIGURE 8 The (a) mass–size and (b) area–size relationship fits for rimed aggregates consisting of monomer needle crystals. The normalized rime mass M of the aggregates is colour coded. Power-law fits for aggregates binned in 10 logarithmic M bins from 10^{-2} to 10^{0} are shown as coloured lines. The fit results in SI units are given in the legend. Unrimed particles ($M = 0$) are included in grey. Results for the other monomer types studied (dendrites, columns, plates, and rosettes) can be found in the Supporting Information.

increasing M, starting at 1.78 for unrimed particles and approaching values of approximately 2 for heavily rimed ones.

Figure 9 summarizes the results of all mass and area–size power-law fits that were performed for the five selected monomer crystal shapes and M levels as well as unrimed aggregates. All parameters increase with increasing amount of riming, however they also show a dependence on monomer shape. Mean values over all monomer types of the mass–size parameter are similar to those of plates. As expected, monomer crystal shape plays a larger role for smaller M, with b_m values for particles in the lowest M bin ranging from 2.17 for columns to 2.52 for dendrites with corresponding a_m values of 0.0988 and 0.388. When a

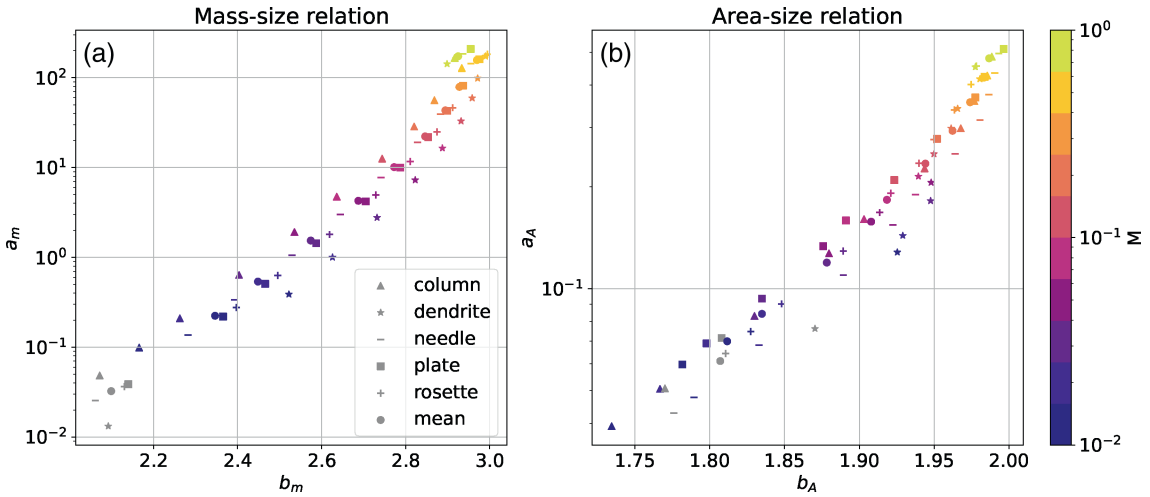

FIGURE 9 Results of the fit parameters of the power-law (a) mass–size and (b) area–size relationship fits for the monomer crystal types studied and normalized rime mass M values. The b parameters are plotted versus the a parameters in SI units. The colour represents the corresponding M bin, results for unrimed particles ($M = 0$) are shown in grey. Monomer crystal types are differentiated by markers: columns correspond to triangles, dendrites to stars, needles to minus signs, plates to squares, and rosettes to plus signs. Mean values over all types for each M bin are plotted as circles.

TABLE 2 Mass–size parameter (a_m, b_m) depending on the normalized rime mass M for the monomer crystal types studied.

M	Columns	Dendrites	Needles	Plates	Rosettes	Mean
0.000	(0.0485, 2.07)	(0.0132, 2.09)	(0.0254, 2.06)	(0.0388, 2.14)	(0.0363, 2.13)	(0.0324, 2.10)
0.013	(0.0988, 2.17)	(0.388, 2.52)	(0.136, 2.28)	(0.219, 2.37)	(0.277, 2.40)	(0.224, 2.35)
0.021	(0.210, 2.26)	(1.00, 2.63)	(0.336, 2.39)	(0.508, 2.47)	(0.629, 2.50)	(0.537, 2.45)
0.033	(0.638, 2.40)	(2.77, 2.73)	(1.05, 2.53)	(1.44, 2.59)	(1.80, 2.62)	(1.54, 2.57)
0.052	(1.91, 2.54)	(7.26, 2.82)	(3.01, 2.64)	(4.20, 2.71)	(4.84, 2.73)	(4.27, 2.69)
0.082	(4.74, 2.64)	(16.4, 2.89)	(7.77, 2.74)	(9.97, 2.79)	(11.6, 2.81)	(10.1, 2.77)
0.129	(12.5, 2.74)	(32.9, 2.93)	(19.1, 2.83)	(21.8, 2.85)	(24.9, 2.87)	(22.2, 2.85)
0.205	(28.6, 2.82)	(59.4, 2.96)	(39.4, 2.88)	(42.8, 2.90)	(46.4, 2.91)	(43.3, 2.89)
0.325	(56.2, 2.87)	(98.6, 2.97)	(78.0, 2.93)	(81.5, 2.94)	(81.0, 2.94)	(79.0, 2.93)
0.515	(128, 2.93)	(173, 2.99)	(143, 2.96)	(160, 2.98)	(182, 2.99)	(157, 2.97)
0.816	(166, 2.92)	(143, 2.90)	(184, 2.94)	(209, 2.95)	(165, 2.92)	(173, 2.93)

Note: All values in SI untis.

particle approaches a graupel-like shape, it does not matter much what monomers the original aggregate was composed of. b_m values for the highest M bin ($M \approx 0.8$) range from 2.90–2.95 and are generally slightly smaller than for the previous bin (2.93–2.99). Here, a bias of D_{max} towards smaller sizes for high M levels could play a role. As mentioned in Section 2.2, the largest aggregates did not reach $M \approx 1$ with the amount of liquid water that they were exposed to. Another explanation could be a "saturation" effect, with particles in the second highest M bin being already so heavily rimed that an increase in rime does not change their properties much. Except for very high M, the mass–size parameters are smallest for columns, followed by needles, plates, and rosettes, and largest for dendrites.

The area–size parameter shows a similar behaviour, with values generally increasing with increasing M. For the highest M bins, the area–size parameters are similar for all monomer shapes (a_A ranges from 0.453–0.512, b_A from 1.98–2.00). However, for unrimed particles they depend heavily on monomer shape. With $b_A = 1.93$, dendrites of the lowest M ($M \approx 0.01$) show a similar area–size relation to needles with medium riming ($M \approx 0.08$: $b_A = 1.94$). All resulting mass and area–size parameters can be found in SI units in Tables 2 and 3.

TABLE 3 Area–size parameter (a_A, b_A) depending on the normalized rime mass M for the monomer crystal types studied.

M	Columns	Dendrites	Needles	Plates	Rosettes	Mean
0.000	(0.0508, 1.77)	(0.0762, 1.87)	(0.0428, 1.78)	(0.0715, 1.81)	(0.0643, 1.81)	(0.0611, 1.81)
0.013	(0.0392, 1.73)	(0.128, 1.93)	(0.0577, 1.79)	(0.0597, 1.78)	(0.0748, 1.83)	(0.0699, 1.81)
0.021	(0.0506, 1.77)	(0.144, 1.93)	(0.0681, 1.83)	(0.0689, 1.80)	(0.0902, 1.85)	(0.0843, 1.83)
0.033	(0.0831, 1.83)	(0.182, 1.95)	(0.110, 1.89)	(0.0935, 1.83)	(0.129, 1.89)	(0.120, 1.88)
0.052	(0.127, 1.88)	(0.206, 1.95)	(0.154, 1.92)	(0.134, 1.88)	(0.168, 1.91)	(0.158, 1.91)
0.082	(0.161, 1.90)	(0.215, 1.94)	(0.190, 1.94)	(0.159, 1.89)	(0.192, 1.92)	(0.183, 1.92)
0.129	(0.227, 1.94)	(0.250, 1.95)	(0.250, 1.96)	(0.210, 1.92)	(0.235, 1.94)	(0.234, 1.94)
0.205	(0.298, 1.97)	(0.298, 1.96)	(0.316, 1.98)	(0.278, 1.95)	(0.276, 1.95)	(0.293, 1.96)
0.325	(0.359, 1.98)	(0.341, 1.97)	(0.375, 1.99)	(0.368, 1.98)	(0.338, 1.96)	(0.356, 1.97)
0.515	(0.427, 1.99)	(0.417, 1.98)	(0.434, 1.99)	(0.423, 1.98)	(0.402, 1.97)	(0.421, 1.98)
0.816	(0.485, 1.99)	(0.453, 1.98)	(0.496, 1.99)	(0.512, 2.00)	(0.455, 1.98)	(0.480, 1.99)

Note: All values in SI untis.

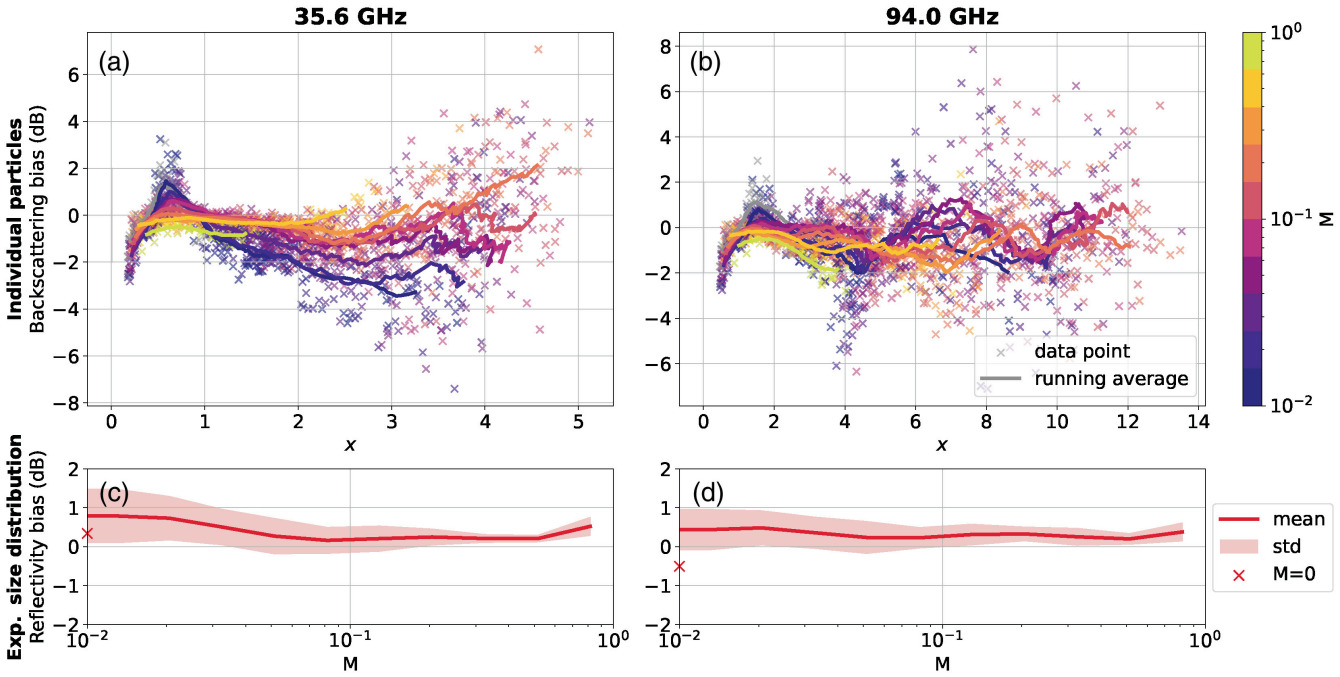

FIGURE 10 (a,b) As Figure 6 and (c,d) as Figure 7, but using the mass–size parameter from Table 2 instead of exact particle masses.

3.5 | Combining M-dependent SSRGA and mass–size parameterizations

In Sections 3.1 and 3.3 we calculated σ_b using the exact particle masses. However, as stated in Section 3.4, exact masses of particles sampled with microwave remote sensing are unknown and mass–size relations are commonly applied. We therefore analyse the accuracy of using the riming-dependent parameterization together with the mass–size relationships presented in the previous section compared with calculating the SSRGA parameter directly and using exact particle masses. Figure 10 shows the σ_b bias for (average) individual particles (as in Figure 6) as well as the reflectivity Z_e bias applying exponential size distributions (as in Figure 7). We use median M values for each size bin and monomer type and interpolate the a_m and b_m from Table 2 with cubic interpolation. For medium and high riming degrees, biases are low (within 1 dB) in the Ka band. However, average σ_b bias for lightly rimed particles with $x > 2.5$ shows a negative bias exceeding

2 dB. This is likely due to the higher variability in structure and larger D_{max} of lightly rimed compared with more heavily rimed particles, leading to higher uncertainties in mass–size relations. Interestingly, biases due to mass–size assumptions and the riming-dependent parameterization seem to compensate each other in the W band, leading to average uncertainties below 2 dB over the full size and M range. Mean Z_e biases applying exponential size distributions stay below 1 dB over all riming levels for both 35.6 and 94.0 GHz.

Comparing Figures 10 with 6d,h, it seems that the bias due to the choice of mass–size relation is at least as large as the bias due to the choice of SSRGA parameters. As we show in the Supporting Information (Figure S13), applying a constant mass–size relation leads to higher biases than varying mass–size but using the SSRGA parameter for a constant M. However, the best performance is achieved when both mass–size and SSRGA parameters are derived as functions of M using the riming-dependent parameterization.

4 | CONCLUSION

In this study, we have developed a parameterization of the SSRGA parameters α_e, κ, β, γ, ζ_1 and the mass and area–size relations $m(D_{max})$ and $a(D_{max})$ by the normalized rime mass M ("the riming-dependent parameterization"). This allows us to estimate the backscattering cross-section of a particle with D_{max} and M. To investigate the relationship between riming and SSRGA scattering, we generated synthetic ice particles with an aggregation and riming model. We obtained a large data set of horizontally aligned rimed aggregates of different sizes and monomer ice-crystal shapes (columns, dendrites, needles, plates, and rosettes; no mixtures), which we binned by M. We then calculated the SSRGA parameter for each monomer type and M over the size spectrum. Via linear discriminant analysis (LDA) and fits, we derived empirical relations of α_e, κ, β, γ, ζ_1 as functions of only M. α_e shows the most correlation with M, whereas κ and ζ_1 are almost constant except for the highest M bin.

We were able to obtain the following results.

1. We confirmed previous findings that the Rayleigh–Gans Approximation (RGA) provides reasonably accurate backscattering cross-section σ_b results compared with the Discrete Dipole Approximation (DDA) for all riming degrees in the Ka band (35.6 GHz). The same holds in the W band (94.0 GHz) for all but very heavily rimed particles with sizes larger than the wavelength (Figure 4). While the bias in backscattering cross-section can be very high for individual particles larger than the wavelength (for all riming degrees), average values stay below 11% or 0.5 dB (1.2 dB for the W band and $M > 0.4$). Also, SSRGA using the riming-dependent parameterization approximates DDA results well for the selected particles (Figure 5).
2. Using the riming-dependent parameterization of the SSRGA parameter instead of values suggested in the literature leads to significantly smaller σ_b biases (compared with the calculated SSRGA parameter, used as reference) for 35.6 and 94.0 GHz. This holds on average for individual particles (Figure 6) as well as particle populations (Figure 7). The running average of the σ_b bias stays below ± 2 dB for the riming-dependent parameterization for all M bins over the full size range studied (up to 10 mm), with the exception of large very lightly rimed particles ($D_{max} > 5$ mm and $M < 0.016$) in the W band. Using literature values leads to average absolute biases of up to 8 dB. In the case of observing particles following an exponential size distribution, mean reflectivity biases calculated using the riming-dependent parameterization are below 0.5 dB in the W band and below 0.05 dB in the Ka band for all riming degrees. We therefore recommend the use of our empirical function when dealing with rimed aggregates. The reader has to be aware of the limits of RGA and further SSRGA for very high M (graupel-like particles) and large particles ($D_{max} > \lambda$), due to increasing interdipole interactions which are neglected.
3. We investigated mass and area–size relationships $m(D_{max})$ and $a(D_{max})$ for different monomer types (columns, dendrites, needles, plates, and rosettes) and riming degrees (see Figures 8 and 9). We found that generally mass–size and area–size parameters (a_m, b_m) and (a_A, b_A) increase with increasing M. However, monomer crystal type plays a role as well, especially for lower riming degrees. b_m values for unrimed aggregates are close to 2 and increase to approximately 3 for high M. b_A values follow a similar behaviour, with values around 1.8 for unrimed and 2.0 for heavily rimed particles. For unrimed and lightly rimed particles, monomer shape plays a larger role than in the mass–size relation. These findings appear to be in contradiction to the classic "fill-in" model. We also see increases in size in earlier riming stages and our results follow closely the modelling results presented in Seifert *et al.* (2019), which is not surprising, due to us employing the same aggregation and riming model. We summarized all fit values in Tables 2 and 3 for $m(D_{max})$ and $a(D_{max})$.
4. Finally, we evaluated the performance of combining the riming-dependent parameterization and the proposed mass–size parameterizations (see Figure 10). The mass–size parameter leads to higher σ_b uncertainties

for unrimed and lightly rimed particles compared with fixing the mass to its exact values, likely due to more variability in particle structures. In the case of applying exponential size distributions, mean σ_b bias stays below 1 dB over all riming degrees for both frequencies.

The proposed framework allows us to estimate backscattering properties of aggregates consistently as a function of their degree of riming, expressed by the normalized rime mass M. The ability to vary M continuously without discrete jumps allows us to apply our method to retrievals and atmospheric models with varying M. It can, for example, be used to forward-model radar reflectivities from atmospheric models that include a microphysical scheme such as the P3 microphysical scheme (Morrison and Milbrandt, 2015).

Our results are purely based on modelled data, and validating these findings based on laboratory experiments or field measurements is important. New laboratory experiments studying the evolution of particle structure during riming are crucial to gain a deeper understanding of the riming process. Also, collocated radar and in situ measurements can provide a way to apply and validate our findings in radar retrievals.

Limitations of the model used are as follows: (1) cloud droplet size is assumed to be monodisperse and (2) aerodynamic effects are neglected. Since all our particles were exposed to the same effective liquid water path (ELWP), larger particles did not reach as high M values as smaller ones. This could have led to a bias towards smaller sizes for large M ($> 10^{-1}$), which should be investigated further in the future. Although we do not expect significant changes in the parameterization of the SSRGA parameter, given the fact that we could not find clear dependences of the parameters on particle size, including large particles with high M in the mass–size and area–size fits could lead to slightly different results for a_m, b_m, a_A, and b_A. Another limitation of our work that should be investigated in the future is the assumption of rime density $\rho_{rime} = 700\ kg \cdot m^{-3}$ (high-density scenario in Seifert *et al.* (2019). In a follow-up study, we could investigate varying ρ_{rime} to see the robustness of the results.

AUTHOR CONTRIBUTIONS

Nina Maherndl: conceptualization; formal analysis; methodology; visualization; writing – original draft; writing – review and editing. **Maximilian Maahn:** conceptualization; funding acquisition; supervision; writing – review and editing. **Frederic Tridon:** conceptualization; software; writing – review and editing. **Jussi Leinonen:** software; writing – review and editing. **Davide Ori:** software; writing – review and editing. **Stefan Kneifel:** conceptualization; writing – review and editing.

ACKNOWLEDGEMENTS

We gratefully acknowledge the funding by the Deutsche Forschungsgemeinschaft (DFG, German Research Foundation) for the "Arctic Amplification: Climate Relevant Atmospheric and Surface Processes, and Feedback Mechanisms" (AC)3 Project 268020496-TRR 172 within the Transregional Collaborative Research Center. Contributions by SK were funded by DFG SPP 2115, Project 408012686 (PROM-POMODORI). Work done by FT was funded by by the US Atmospheric System Research (grant no. DESC001796). DO receives financial support from the German Research Foundation (DFG) under the grant SCHE 2074/1-1 (SPP-HALO) and the project 492274454 (PRISTINE SPP-PROM). Open Access funding enabled and organized by Projekt DEAL.

CONFLICT OF INTEREST STATEMENT

The authors declare no conflict of interest.

DATA AVAILABILITY STATEMENT

The data set of simulated rimed aggregates generated for this study is available at https://doi.org/10.5281/zenodo.7757034 (Maherndl *et al.*, 2023).

ORCID

Nina Maherndl https://orcid.org/0000-0003-1517-1534
Maximilian Maahn https://orcid.org/0000-0002-2580-9100
Jussi Leinonen https://orcid.org/0000-0002-6560-6316
Davide Ori https://orcid.org/0000-0002-9964-2200

REFERENCES

Bohren, C. and Huffman, D. (1983) *Absorption and Scattering of Light by Small Particles*. New York: Wiley.

Brown, P.R.A. and Francis, P.N. (1995) Improved measurements of the ice water content in cirrus using a total-water probe. *Journal of Atmospheric and Oceanic Technology*, 12, 410–414 https://journals.ametsoc.org/view/journals/atot/12/2/1520-0426_1995_012_0410_imotiw_2_0_co_2.xml.

Draine, B.T. and Flatau, P.J. (1994) Discrete-dipole approximation for scattering calculations. *Journal of the Optical Society of America*, 11, 1491–1499 https://opg.optica.org/josaa/abstract.cfm?uri=josaa-11-4-1491.

Erfani, E. and Mitchell, D.L. (2017) Growth of ice particle mass and projected area during riming. *Atmospheric Chemistry and Physics*, 17, 1241–1257 https://acp.copernicus.org/articles/17/1241/2017/.

Field, P.R., Hogan, R.J., Brown, P.R.A., Illingworth, A.J., Choularton, T.W. and Cotton, R.J. (2005) Parametrization of ice-particle size distributions for mid-latitude stratiform cloud. *Quarterly Journal of the Royal Meteorological Society*, 131, 1997–2017 https://onlinelibrary.wiley.com/doi/abs/10.1256/qj.04.134.

Harimaya, T. and Sato, M. (1989) Measurement of the riming amount on snowflakes. *Journal of the Faculty of Science, Hokkaido University*, 8, 355–366.

Heymsfield, A.J. (1982) A comparative study of the rates of development of potential Graupel and hail embryos in high plains storms. *Journal of the Atmospheric Sciences*, 39, 2867–2897 https://journals.ametsoc.org/view/journals/atsc/39/12/1520-0469_1982_039_2867_acsotr_2_0_co_2.xml.

Hogan, R.J., Honeyager, R., Tyynelä, J. and Kneifel, S. (2017) Calculating the millimetre-wave scattering phase function of snowflakes using the self-similar Rayleigh–Gans approximation. *Quarterly Journal of the Royal Meteorological Society*, 143, 834–844 https://onlinelibrary.wiley.com/doi/abs/10.1002/qj.2968.

Hogan, R.J. and Westbrook, C.D. (2014) Equation for the microwave backscatter cross section of aggregate snowflakes using the self-similar Rayleigh–Gans approximation. *Journal of the Atmospheric Sciences*, 71, 3292–3301 https://journals.ametsoc.org/view/journals/atsc/71/9/jas-d-13-0347.1.xml.

Kneifel, S. and Moisseev, D. (2020) Long-term statistics of riming in nonconvective clouds derived from ground-based Doppler cloud radar observations. *Journal of the Atmospheric Sciences*, 77, 3495–3508 https://journals.ametsoc.org/view/journals/atsc/77/10/jasD200007.xml.

Leinonen, J., Kneifel, S. and Hogan, R.J. (2018) Evaluation of the Rayleigh–Gans approximation for microwave scattering by rimed snowflakes. *Quarterly Journal of the Royal Meteorological Society*, 144, 77–88 https://onlinelibrary.wiley.com/doi/abs/10.1002/qj.3093.

Leinonen, J. and Moisseev, D. (2015) What do triple-frequency radar signatures reveal about aggregate snowflakes? *Journal of Geophysical Research: Atmospheres*, 120, 229–239 https://onlinelibrary.wiley.com/doi/abs/10.1002/2014JD022072.

Leinonen, J., Moisseev, D. and Nousiainen, T. (2013) Linking snowflake microstructure to multi-frequency radar observations. *Journal of Geophysical Research: Atmospheres*, 118, 3259–3270 https://onlinelibrary.wiley.com/doi/abs/10.1002/jgrd.50163.

Leinonen, J. and Szyrmer, W. (2015) Radar signatures of snowflake riming: a modeling study. *Earth and Space Science*, 2, 346–358 https://agupubs.onlinelibrary.wiley.com/doi/abs/10.1002/2015EA000102.

Locatelli, J.D. and Hobbs, P.V. (1974) Fall speeds and masses of solid precipitation particles. *Journal of Geophysical Research (1896-1977)*, 79, 2185–2197 https://onlinelibrary.wiley.com/doi/abs/10.1029/JC079i015p02185.

Lowenthal, D.H., Borys, R.D., Cotton, W., Saleeby, S., Cohn, S.A. and Brown, W.O.J. (2011) The altitude of snow growth by riming and vapor deposition in mixed-phase orographic clouds. *Atmospheric Environment*, 45, 519–522 https://www.sciencedirect.com/science/article/pii/S1352231010008472.

Maahn, M. and Löhnert, U. (2017) Potential of higher-order moments and slopes of the radar Doppler spectrum for retrieving microphysical and kinematic properties of arctic ice clouds. *Journal of Applied Meteorology and Climatology*, 56, 263–282 https://journals.ametsoc.org/view/journals/apme/56/2/jamc-d-16-0020.1.xml.

Maahn, M., Löhnert, U., Kollias, P., Jackson, R.C. and McFarquhar, G.M. (2015) Developing and evaluating ice cloud parameterizations for forward modeling of radar moments using in situ aircraft observations. *Journal of Atmospheric and Oceanic Technology*, 32, 880–903 https://journals.ametsoc.org/view/journals/atot/32/5/jtech-d-14-00112_1.xml.

Maherndl, N., Maahn, M., Tridon, F., Leinonen, J., Ori, D. and Kneifel, S. (2023) Data set of simulated rimed aggregates for "A riming-dependent parameterization of scattering by snowflakes using the self-similar Rayleigh-Gans approximation". https://doi.org/10.5281/zenodo.7757034.

Mason, S.L., Chiu, C.J., Hogan, R.J., Moisseev, D. and Kneifel, S. (2018) Retrievals of riming and snow density from vertically pointing Doppler radars. *Journal of Geophysical Research: Atmospheres*, 123, 13807–13834 https://onlinelibrary.wiley.com/doi/abs/10.1029/2018JD028603.

Mason, S.L., Hogan, R.J., Westbrook, C.D., Kneifel, S., Moisseev, D. and von Terzi, L. (2019) The importance of particle size distribution and internal structure for triple-frequency radar retrievals of the morphology of snow. *Atmospheric Measurement Techniques*, 12, 4993–5018 https://amt.copernicus.org/articles/12/4993/2019/.

McCusker, K., Westbrook, C.D. and Tyynelä, J. (2021) An accurate and computationally cheap microwave scattering method for ice aggregates: the independent monomer approximation. *Quarterly Journal of the Royal Meteorological Society*, 147, 1202–1224 https://onlinelibrary.wiley.com/doi/abs/10.1002/qj.3967.

McLachlan, G.J. (2005) *Discriminant Analysis and Statistical Pattern Recognition*. Wiley-Interscience Paperback Series, 1. aufl. edition. Hoboken: Wiley-Interscience.

Mech, M., Maahn, M., Kneifel, S., Ori, D., Orlandi, E., Kollias, P., Schemann, V. and Crewell, S. (2020) PAMTRA 1.0: the passive and active microwave radiative TRAnsfer tool for simulating radiometer and radar measurements of the cloudy atmosphere. *Geoscientific Model Development*, 13, 4229–4251 https://gmd.copernicus.org/articles/13/4229/2020/.

Mie, G. (1908) Beiträge zur Optik trüber Medien, speziell kolloidaler Metallösungen. *Annalen der Physik*, 330, 377–445 https://onlinelibrary.wiley.com/doi/abs/10.1002/andp.19083300302.

Mishchenko, M.I. (2000) Calculation of the amplitude matrix for a nonspherical particle in a fixed orientation. *Applied Optics*, 39, 1026–1031 https://opg.optica.org/ao/abstract.cfm?uri=ao-39-6-1026.

Mitchell, D.L. (1996) Use of mass- and area-dimensional power laws for determining precipitation particle terminal velocities. *Journal of the Atmospheric Sciences*, 53, 1710–1723 https://journals.ametsoc.org/view/journals/atsc/53/12/1520-0469_1996_053_1710_uomaad_2_0_co_2.xml.

Moisseev, D., von Lerber, A. and Tiira, J. (2017) Quantifying the effect of riming on snowfall using ground-based observations. *Journal of Geophysical Research: Atmospheres*, 122, 4019–4037 https://onlinelibrary.wiley.com/doi/abs/10.1002/2016JD026272.

Morrison, H. and Milbrandt, J.A. (2015) Parameterization of cloud microphysics based on the prediction of bulk ice particle properties. Part I: scheme description and idealized tests. *Journal of the Atmospheric Sciences*, 72, 287–311 https://journals.ametsoc.org/view/journals/atsc/72/1/jas-d-14-0065.1.xml.

Mosimann, L. (1995) An improved method for determining the degree of snow crystal riming by vertical Doppler radar. *Atmospheric Research*, 37, 305–323 https://www.sciencedirect.com/science/article/pii/016980959400050N.

Mosimann, L., Weingartner, E. and Waldvogel, A. (1994) An analysis of accreted drop sizes and mass on rimed snow crystals. *Journal of the Atmospheric Sciences*, 51, 1548–1558 https://journals.

ametsoc.org/view/journals/atsc/51/11/1520-0469_1994_051_1548_aaoads_2_0_co_2.xml.

Mülmenstädt, J., Sourdeval, O., Delanoë, J. and Quaas, J. (2015) Frequency of occurrence of rain from liquid-, mixed-, and ice-phase clouds derived from A-train satellite retrievals. *Geophysical Research Letters*, 42, 6502–6509 https://onlinelibrary.wiley.com/doi/abs/10.1002/2015GL064604.

Myagkov, A., Kneifel, S. and Rose, T. (2020) Evaluation of the reflectivity calibration of W-band radars based on observations in rain. *Atmospheric Measurement Techniques*, 13, 5799–5825 https://amt.copernicus.org/articles/13/5799/2020/.

Nowell, H., Liu, G. and Honeyager, R. (2013) Modeling the microwave single-scattering properties of aggregate snowflakes. *Journal of Geophysical Research: Atmospheres*, 118, 7873–7885 https://onlinelibrary.wiley.com/doi/abs/10.1002/jgrd.50620.

Ori, D., von Terzi, L., Karrer, M. and Kneifel, S. (2021) snowScatt 1.0: consistent model of microphysical and scattering properties of rimed and unrimed snowflakes based on the self-similar Rayleigh–Gans approximation. *Geoscientific Model Development*, 14, 1511–1531 https://gmd.copernicus.org/articles/14/1511/2021/.

Pedregosa, F., Varoquaux, G., Gramfort, A., Michel, V., Thirion, B., Grisel, O., Blondel, M., Prettenhofer, P., Weiss, R., Dubourg, V., Vanderplas, J., Passos, A., Cournapeau, D., Brucher, M., Perrot, M. and Duchesnay, É. (2011) Scikit-learn: machine learning in python. *Journal of Machine Learning Research*, 12, 2825–2830 http://jmlr.org/papers/v12/pedregosa11a.html.

Pruppacher, H.R. and Klett, J. (1997) Atmospheric and oceanographic sciences library. In: *Microphysics of Clouds and Precipitation*, Vol. 18, 2nd edition. Dordrecht: Kluwer.

Seifert, A., Leinonen, J., Siewert, C. and Kneifel, S. (2019) The geometry of rimed aggregate snowflakes: a modeling study. *Journal of Advances in Modeling Earth Systems*, 11, 712–731 https://onlinelibrary.wiley.com/doi/abs/10.1029/2018MS001519.

Tian, L., Heymsfield, G.M., Li, L., Heymsfield, A.J., Bansemer, A., Twohy, C.H. and Srivastava, R.C. (2010) A study of cirrus ice particle size distribution using TC4 observations. *Journal of the Atmospheric Sciences*, 67, 195–216 https://journals.ametsoc.org/view/journals/atsc/67/1/2009jas3114.1.xml.

Tridon, F., Silber, I., Battaglia, A., Kneifel, S., Fridlind, A., Kalogeras, P. and Dhillon, R. (2022) Highly supercooled riming and unusual triple-frequency radar signatures over Antarctica. *Atmospheric Chemistry and Physics*, 22, 12467–12491 https://doi.org/10.5194/acp-22-12467-2022.

Tyynelä, J., Leinonen, J., Westbrook, C.D., Moisseev, D. and Nousiainen, T. (2013) Applicability of the Rayleigh-Gans approximation for scattering by snowflakes at microwave frequencies in vertical incidence. *Journal of Geophysical Research: Atmospheres*, 118, 1826–1839 https://onlinelibrary.wiley.com/doi/abs/10.1002/jgrd.50167.

Vogl, T., Maahn, M., Kneifel, S., Schimmel, W., Moisseev, D. and Kalesse-Los, H. (2022) Using artificial neural networks to predict riming from Doppler cloud radar observations. *Atmospheric Measurement Techniques*, 15, 365–381 https://amt.copernicus.org/articles/15/365/2022/.

Warren, S.G. and Brandt, R.E. (2008) Optical constants of ice from the ultraviolet to the microwave: a revised compilation. *Journal of Geophysical Research: Atmospheres*, 113, D14220, https://onlinelibrary.wiley.com/doi/abs/10.1029/2007JD009744.

Westbrook, C.D. (2014) Rayleigh scattering by hexagonal ice crystals and the interpretation of dual-polarisation radar measurements. *Quarterly Journal of the Royal Meteorological Society*, 140, 2090–2096 https://onlinelibrary.wiley.com/doi/abs/10.1002/qj.2262.

Westbrook, C.D., Ball, R.C., Field, P.R. and Heymsfield, A.J. (2004) Universality in snowflake aggregation. *Geophysical Research Letters*, 31, L15104, https://onlinelibrary.wiley.com/doi/abs/10.1029/2004GL020363.

Wood, N.B., L'Ecuyer, T.S., Heymsfield, A.J., Stephens, G.L., Hudak, D.R. and Rodriguez, P. (2014) Estimating snow microphysical properties using collocated multisensor observations. *Journal of Geophysical Research: Atmospheres*, 119, 8941–8961 https://onlinelibrary.wiley.com/doi/abs/10.1002/2013JD021303.

Yurkin, M.A. and Hoekstra, A.G. (2011) The discrete-dipole-approximation code ADDA: capabilities and known limitations. *Journal of Quantitative Spectroscopy and Radiative Transfer*, 112, 2234–2247 https://www.sciencedirect.com/science/article/pii/S0022407311000562.

Yurkin, M.A., Maltsev, V.P. and Hoekstra, A.G. (2007) The discrete dipole approximation for simulation of light scattering by particles much larger than the wavelength. *Journal of Quantitative Spectroscopy and Radiative Transfer*, 106, 546–557 https://www.sciencedirect.com/science/article/pii/S0022407307000544.

Zubko, E., Petrov, D., Grynko, Y., Shkuratov, Y., Okamoto, H., Muinonen, K., Nousiainen, T., Kimura, H., Yamamoto, T. and Videen, G. (2010) Validity criteria of the discrete dipole approximation. *Applied Optics*, 49, 1267–1279.

SUPPORTING INFORMATION

Additional supporting information can be found online in the Supporting Information section at the end of this article.

How to cite this article: Maherndl, N., Maahn, M., Tridon, F., Leinonen, J., Ori, D. & Kneifel, S. (2023) A riming-dependent parameterization of scattering by snowflakes using the self-similar Rayleigh–Gans approximation. *Quarterly Journal of the Royal Meteorological Society*, 149(757), 3562–3581. Available from: https://doi.org/10.1002/qj.4573